Microseismic Cloud Growth Process Mainly Controlled by *In-Situ* Stress During Hydraulic Stimulation

Y. Mukuhira[1], M. Yang[1,2], K. Okamoto[3], T. Ishibashi[3], Y. Kumano[4], H. Moriya[5], T. Ito[1], H. Asanuma[4], K. Yan[1,2], Y. Zuo[2], J. Rubinstein[6], M. O. Häring[7]

[1]Institute of Fluid Science, Tohoku University.

[2]State Key Laboratory of Oil and Gas Geology and Exploitation, Chengdu University of Technology.

[3]Fukushima Renewable Energy Institute, National Institute of Advanced Industrial Science and Technology

[4]JAPEX Co., Ltd.

[5]School of engineering, Tohoku University.

[6]United States Geological Survey.

[7]Häring GeoProject.

Corresponding author: Yusuke Mukuhira (mukuhira@tohoku.ac.jp)

Key Points:

- Microseismic cloud shape changed before and after stimulation, suggesting a difference in the dynamic and static permeability tensor.
- Microseismic cloud growth behavior is mainly controlled by *in-situ* stress when existing fractures have enough variations in their orientation.
- The shape of the microseismic cloud relates to the *in-situ* stress ratio, which may be used to design an energy extraction system.

Abstract

Forecasting the shape of a microseismic cloud is essential to pre-design an energy extraction system. The microseismic cloud produced after hydraulic stimulation is empirically known to extend to the maximum principal stress direction. However, this empirical relationship is inconsistent with the results of some studies, and the cloud growth process has not been fully understood. This study investigates the microseismic cloud growth process using microseismic data derived from a stimulation in Basel, Switzerland and considering its correlation with *in-situ* stress. We applied principal component analysis to a time series of microseismic distribution for macroscopic characterization of microseismic cloud growth. The least orientation of the microseismic cloud was stable and almost identical to minimum horizontal stress. The most extensive orientation experienced some dip angle during stimulation, although it had become almost vertical following injection. This suggests that microseismic cloud growth behavior was different before and after stimulation, owing to the dynamic and static permeability tensor. There was radial growth in the cross-sectional microseismic cloud along with the maximum horizontal stress orientation. This is consistent with the nearly identical maximum horizontal and vertical stresses. Microseismic clouds did not grow in the least principal stress direction due to low permeability. However, the microseismic cloud extended between the orientation of the maximum and intermediate stresses, reflecting their magnitude. These findings suggest that microseismic cloud growth is mainly controlled by *in-situ* stress when various existing faults exist. They also suggest the feasibility of forecasting microseismic reservoir shape from *in-situ* stress before stimulation.

Plain Language Summary

1 Introduction

In the new plague era, a supply of stable energy is critically important to sustainably maintain broad economic and social activities. Additionally, the transition from hydrocarbon resources associated with carbon dioxide (CO_2) emissions to renewable energy is necessary to mitigate global warming and various risks associated with global warming. Geothermal energy is one of the most promising renewable energy sources as its stability is suitable for baseload. There have been many attempts to increase geothermal energy use even in a non-volcanic region, through an enhanced geothermal system (EGS). In EGS development, we extract geothermal energy from deeper than the volcanic region to access economically competitive temperatures. Based on the permeability and fluid richness condition in the target formation, an engineering operation was employed to increase the permeability or feed fluid of the heat exchange medium; that is, the hydraulic stimulation (hydro shearing). The injected water migrates via the existing fracture system in the reservoir, and the increased pore pressure concurrently destabilizes each existing fault. When friction decreases to a sufficient amount to yield shear stress, shear slip occurs on existing fractures (Pine & Batchelor, 1984; Zoback, 2007), resulting in microseismicity. This is the main part of the EGS engineering operation as shear slips on existing fractures enhances permeability (Watanabe et al., 2008; Yeo et al., 1998). Measurement and analysis of microseismicity are also essential parts of EGS, involving the monitoring of hydraulic stimulation and visualization of the shape and geometry of the artificial reservoirs. Microseismic data are often automatically processed, and the hypocenter locations of microseismicity are routinely determined using automatically detected P and S-wave arrival. Due to uncertainty in the phase arrival, microseismic hypocenters often show a cloud shape (i.e., the microseismic cloud, herein referred as the MS cloud). Post analysis by experts includes refined phase picking, relocation of the hypocenter, estimating the source parameter, and focal mechanisms. Relocated hypocenter determinations delineate a much sharper existing fracture system as opposed to an ambiguous MS cloud.

The shape or geometry of the EGS reservoir from microseismic monitoring is very important in the design of sustainable energy extraction systems. This indicates the location of production wells, the entire rock volume available for heat exchange, and reservoir management. It has been considered that the MS cloud grows in the maximum principal stress direction of, although this has not yet been proven; as such, the MS cloud growth process is not been fully understood. The model for earthquake swarms in a volcanic region (Hill, 1977) has often been used to interpret MS cloud growth (Evans et al., 2005; Häring et al., 2008). A similar model was also proposed by Sibson (1996). In these models, the conjugate faults and dikes consist of the fracture mesh model. At stimulation, optimally oriented faults to *in-situ* stress initially cause shear slip with a minimum pore pressure increase. However, optimally oriented faults have angles around 30° to the orientation of maximum principal stress; this is not the same orientation as the maximum principal stress. Microseismic events often occur from both conjugates of optimally oriented faults. Consequently, the MS cloud grows in the direction of maximum principal stress from a macroscopic perspective, as presented in Häring et al. (2008).

This empirical interpretation does not always explain the observed MS cloud shape. For the EGS reservoir of Basel, Switzerland and Soultz, France, both of which are from the Rhine graben, the shape of the MS cloud was consistent with the maximum principal stress orientation (Evans et al., 2005; Häring et al., 2008; Mukuhira et al., 2013; Soma et al., 2007). As a counter-example, the hot fracture rock (HFR) project in the Cooper Basin, Australia had different features. The MS cloud mainly consists of one or a few sub-horizontal fractures, and they delineate thin and planar MS clouds (Baisch et al., 2006). The planar MS cloud did not grow to the maximum principal stress orientation. Thus, the MS cloud of the Cooper Basin is heavily controlled by the dominant horizontal existing fractures as opposed to *in-situ* stress. Another counter-example is the case of the Fenton Hill HDR test site in the United States. The MS cloud clearly did not extend to the maximum principal stress orientation (Norbeck et al., 2018). These examples demonstrate that MS cloud growth behavior has not yet been fully understood, and further clarification on its correlation to *in-situ* stress, existing fracture distribution, and pore pressure is required.

This study investigates MS cloud growth behavior and the influence of *in-situ* stress. It utilizes well-recorded microseismicity, *in-situ* stress, and existing fracture data from the case study EGS project in Basel, Switzerland. Then, it discusses whether the insights from the analysis of this case study may explain MS cloud growth behavior of other fields based on the distinction between *in-situ* stress and existing fracture data.

2 Data and Methods

2.1 Field description

We studied microseismic activity observed at the hydraulic stimulation of the EGS project in Basel, Switzerland, in 2006. The EGS project used hydraulic stimulation to create an artificial geothermal reservoir for electricity and heat supply as a cogeneration system. Basel is located at the southern end of the Upper Rhine graben, characterized by the highest geothermal potential in Europe (Figure 1). The injection well, Basel-1, was drilled in the urban part of the city, to a depth of approximately 5000 m from the surface. Following the sedimentary part up to 2500 m, the granite basement formation had begun beyond this depth. The casing shoe was approximately 4630 m, and the remaining 400 m of the open-hole section was subjected to stimulation. Injected water penetrated the formation via several permeable zones in the open-hole section (Häring et al., 2008). Hydraulic stimulation was conducted for approximately five days, beginning on December 2, 2006. The maximum flow rate was 3300 L/min, accompanied by a wellhead pressure reaching 29.6 MPa. Hydraulic stimulation successfully caused numerous microseismicities. Seismic activity increased with flow rate and wellhead pressure, and the MS cloud was extended with the hydraulic stimulation process. On the fifth day of hydraulic stimulation, microseismic activity had been raised unfavorably. Despite efforts to reduce the flow rate and seismic activity, several felt events, including the largest event (Mw 3.41), occurred during the shut-in phase (Häring et al., 2008; Mukuhira et al., 2013). Microseismic activity continued even after half a year following the commencement of stimulation (Mukuhira et al., 2013), and seismic activity is continuing to occur (Herrmann et al., 2019).

2.2 Microseismic data

The primary operator, Geothermal Explorers Ltd. (GEL), installed a microseismic network consisting of six downhole seismometers and one temporal sensor in the injection well (Figure 1). The deepest seismometer, Otterbach 1 (OT1), was installed at the top of the granite section, and other seismometers were in the sediment. One geophone was deployed in Basel1 at 4720 m from the surface. This attempt was intended to acquire the signal of events that occurred at the very early stage of stimulation, assuming that those events occurred within 100 m from the injection point. The data from these events were used to calibrate the initial velocity model estimated from P and S-wave velocities based on sonic velocity measurements. Following this, a one-dimensional (1D) and one layer (i.e., between sediment and granite) velocity model was used for hypocenter determination by GEL (Dyer et al., 2008).

Once the amplitude exceeded the predetermined threshold based on the background noise at the OT1 station, the 6 s waveforms at all stations were flagged as potential events. Then, P and S-wave arrivals were automatically detected and sent to the hypocenter determination process. The initial hypocenter was determined using the grid-based migration method, and events with an RMS misfit of more than 10 ms were discarded. Until the tenth day from the beginning of stimulation, the microseismic monitoring system detected around 13 500 triggers of potential events, whereby ~3100 events were located. Dyer et al. (2010) improved the hypocenter location of microseismic events by applying cross-correlation picking and multiplet analysis.

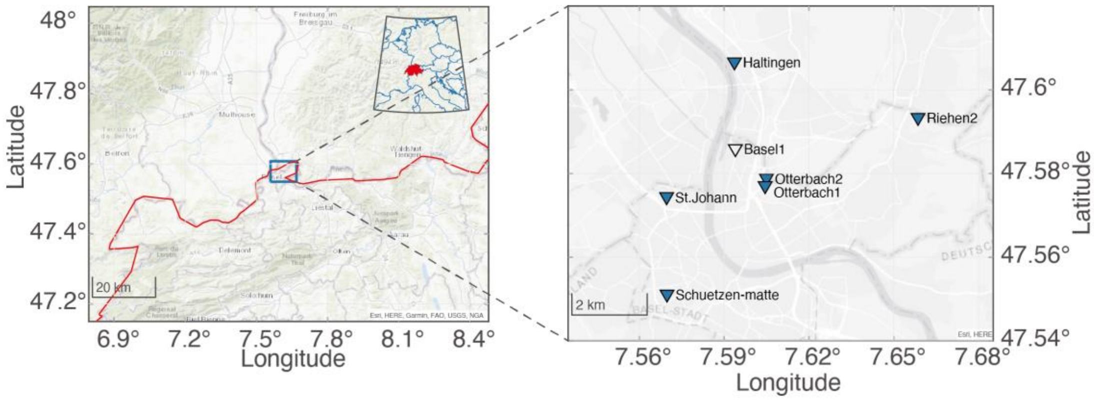

Figure 1. The location of the Basel Switzerland in the left panel, and the microseismic monitoring network of Basel EGS project in Basel city (blue triangles). The open triangle represents the location of the Basel1, injection well.

Asanuma et al. (2007) provided an independent analysis using the same velocity model and a manually refined pick. They then determined the hypocenter location that was almost identical to that found by Dyer et al. (2008). They also applied multiplet analysis and found that 70% of microseismic events were multiplets. Relocated hypocenters using a double difference method (Waldhauser & Ellsworth, 2000) delineated several sub-fractures in the reservoir (Asanuma et al., 2008). This study was based on the hypocenter location elucidated by Asanuma et al. (2008). The spatial error in the hypocenters of absolute locations was approximately 40 m, corresponding to 5 ms in RMS, and the relative error was less than 10 m. The error distribution based on the microseismic monitoring network showed a vertical ellipsoid that was satisfiable compared to other cases (Asanuma et al., 2007). The MS cloud had a sub-vertical geometry striking the NNW-SSE direction in a macroscopic sense.

Figure 2 shows the macroscopic overview of the MS cloud in three dimensions for the stimulation (~shut-in) and post-injection (6 months) time periods. Microseismic activity had commenced near the injection point and expanded in all directions. During the shut-in and bleeding off phase (~5 d from the shut-in), pore pressure re-distribution occurred. This caused very active microseismic activity in the periphery of the previously stimulated region (see details in Mukuhira et al., 2017). Post-stimulation microseismic activity is shown in Figure 2(c) and 2(d). Following the shut-in phase, microseismic activity had become gradual, and microseismic events mostly occurred from the shallower part of the reservoir (Figure 2(d)). Our data included microseismic activity until the 180th day from the commencement of stimulation; continuous microseismic activity has previously been observed even after a decade from stimulation (Herrmann et al., 2019).

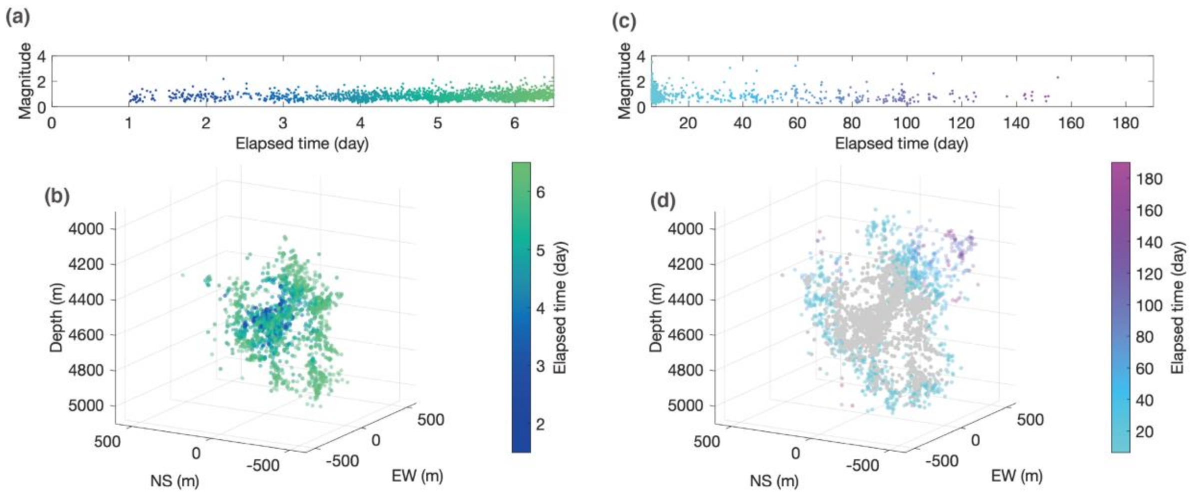

Figure 2. a) Magnitude-time (M-t) plot for stimulation period; and c) until the half-year from stimulation. The color in the M-t plot indicates the occurrence time of each microseismicity; b) and d) three-dimensional panels show the hypocenter distribution of microseismic events for each time period. The color corresponds to the occurrence time of events from the beginning of injection. The gray dots in d) show the hypocenters of events shown in the left panel.

2.3 Principal component analysis

We employed principal component analysis (PCA) to the MS cloud to characterize the MS cloud shape quantitatively and statistically. PCA is a data analysis technique to understand data, and is applicable even to high dimensional data. PCA analysis can also decompose high dimensional data to lower dimensions, and has often recently been used in unsupervised machine learning analysis. In practice, principal components in this case are computed by eigen decomposition of the data covariance matrix, and principal components are considered eigenvectors of the covariance matrix. We applied PCA analysis to microseismic hypocenters consisting of the MS cloud and then extracted the three principal components to understand the hypocenter distribution of microseismic events. The microseismic hypocenter variance was at its maximum along with the first principal component, which means that the MS cloud had extended to the direction of the first principal component.

Effectively, PCA analysis with three orthogonal bases attempts to model the MS cloud with an ellipsoid defined with three component vectors as three axes. The lengths of each axis of the ellipsoid may be estimated assuming the dataset adopts a Gaussian distribution to each axis. In this case, the lengths of each axis were computed as the square root of variance by a factor of three; the ellipsoid defined in this way should include 99 % of microseismic events. The uncertainty of the hypocenter would not affect the PCA results as the error ellipsoid shape for each event in the reservoir was more or less similar (Asanuma et al., 2007). PCA treats the distribution of microseismicity in a macroscopic way, and even considerable uncertainty for one particular event does not materially impact the PCA. It should be noted that the principal components in this analysis were defined as left-handed coordinate systems.

2.4 *In-situ* stress data

The orientation and magnitude of the *in-situ* stress have been investigated using borehole logging data (Valley & Evans, 2009, 2015, 2019). Based on borehole logging analysis, the orientation of the maximum horizontal stress was estimated to be N144°E±14° based on borehole breakout and drilling-induced tensile fracture data (Valley and Evans, 2009). In previous studies (e.g., Mukuhira et al., 2018), we used the *in-situ* stress magnitude model proposed by Valley and Evans (2015). Recently, Valley and Evans (2019) revised the *in-situ* stress magnitude based on careful and comprehensive consideration of borehole breakout, drilling induced tensile fracture, and several failure criteria. The linear depth trends of stress magnitude proposed by Valley and Evans (2019) were $Sv=24.9z$, $S_{hmin}=7\times z + 42$, and $S_{Hmax}=5\times z + 90$; the unit of stress is MPa, and z is the depth from the surface. This small gradient, S_{Hmax}, leads to the stress state transition at 4200 m from strike-slip to normal faulting below. The estimated *in-situ* stress model was consistent with the observed mix of strike-slip and normal fault-type focal mechanisms of larger induced seismic events (Deichmann and Giardini, 2009). We use this *in-situ* stress model, assuming a laterally homogeneous reservoir region for comparison to MS cloud growth and interpretation. Note that this *in-situ* stress itself does not affect the results of the analysis.

3 Results

3.1 Three dimensional MS cloud growth

First, we focused on MS cloud growth during the stimulation period, from the beginning of the stimulation to the shut-in. We computed three PCA components of the MS cloud every 0.5 d. The MS cloud of each time step included all microseismic events that occurred before the target time. Figure 3 shows the three dimensional (3D) microseismic distribution for each time step and the ellipsoids defined with three PCA components. The distribution of microseismic events changed with time; however, the ellipsoids shown in Figure 3 did not change significantly. The orientations of the first and second PCA components, depicted by the red and yellow arrows, dynamically changed with time. The first PCA component was more horizontal in the early few days and commenced dipping around 45° from the horizontal on the third day. The first and second components were more or less constant during the stimulation. It should be noted that PCA estimates the orientation of the first and second components based on the entire data distribution. At times, the direction of components switches 180° according to the local and temporal progress of the MS cloud. Figure 3 shows that the first and second components switched the directions at 4.5 and 5 d. Still, we did not consider the orientation of the arrow in this analysis due to symmetricalness to *in-situ* stress. At the last time step of 6.5 d, the orientation of the first and second PCA components changed, exhibiting different behavior compared to that during stimulation. It should be noted that wellhead pressure decreased due to flow rate reduction from 6 to ~6.5 d. As such, the microseismic activity in this time period was not the same as that during stimulation, based on the pore pressure migration behavior (Mukuhira et al., 2017).

The orientation of the computed PCA components are summarized in the lower hemisphere plot in Figure 4(a)–4(c); the time series change of MS cloud growth orientation is represented. We observed that in the third PCA component, the least orientation of MS cloud growth was constant and almost identical to the minimum horizontal stress, S_{hmin}. In contrast, the first and second PCA components changed in the plane perpendicular to the orientation of S_{hmin}. As observed in Figure 3, the first PCA components were oriented horizontally, then dipped around 45° mid stimulation, and finally ended at a near vertical orientation. Figure 4(d) shows the time series changes of each PCA component length, whilst Figure 4(e) shows the aspect ratio of the ellipse defined for the first and second PCA components to the third one. The first and second PCA components were nearly similar in length throughout the stimulation period. In contrast, the third PCA component grew up to 120 m at most, this was around one-fourth of the other PCA components. The aspect ratios between components varied together between 2.5 and 4. The result of PCA analysis for incremental time step is shown in Figure S1, the result is almost same to those shown here.

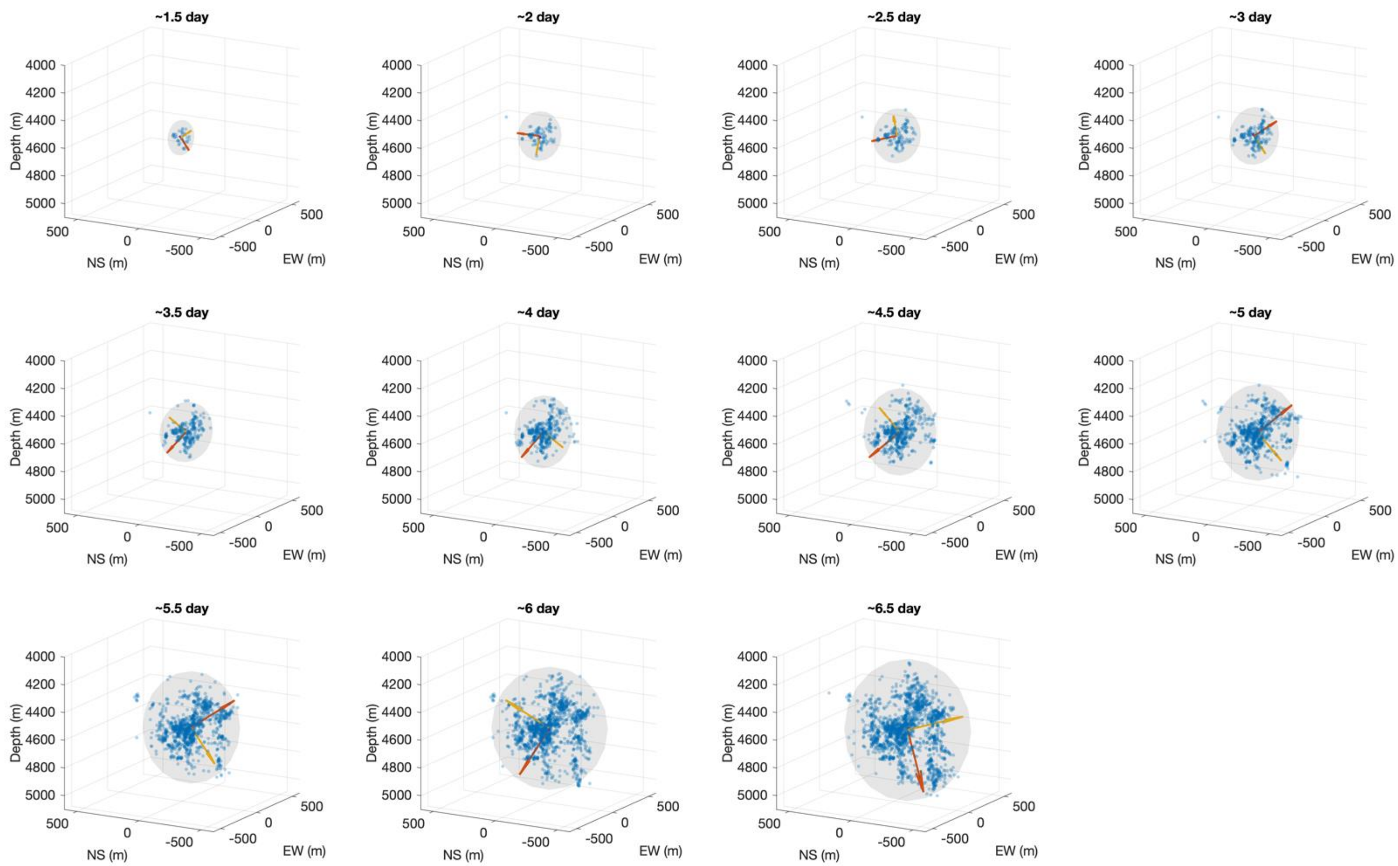

Figure 3. Snapshots of the 3D hypocenter distribution of microseismic events taken every 0.5 d from the beginning of stimulation. The red, yellow, and purple arrows correspond to the first, second and third PCA analysis components that describe representative ellipsoids for MS clouds at each time.

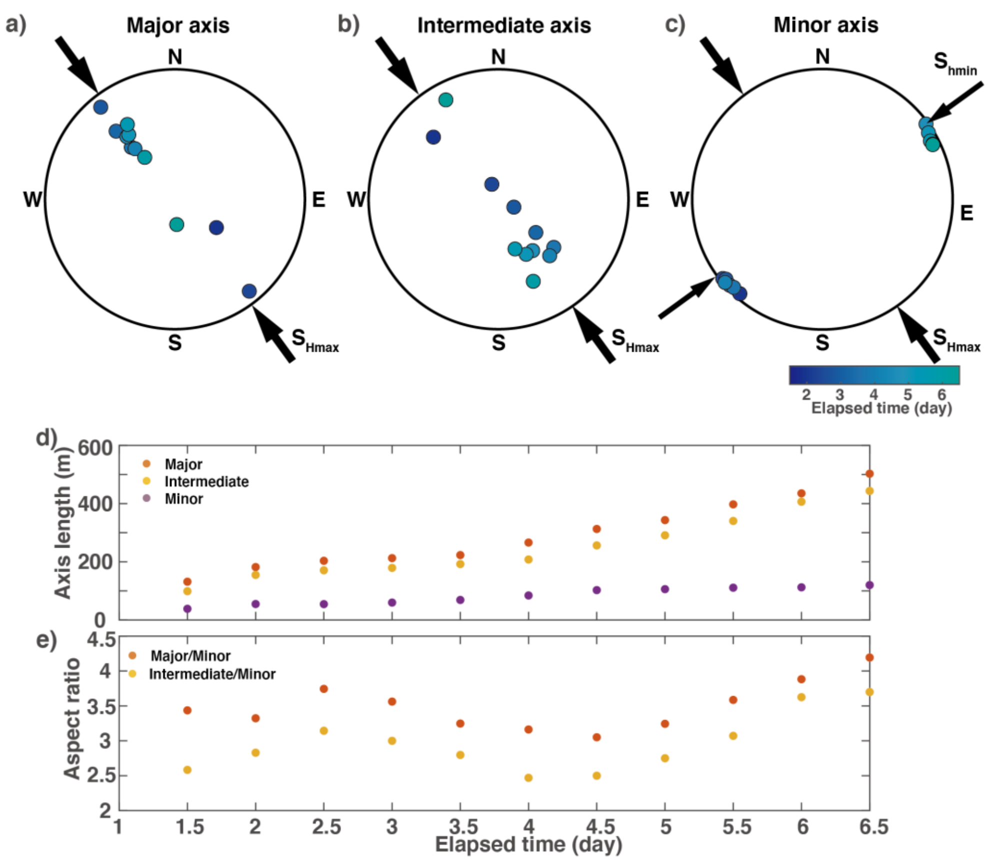

Figure 4. Time series change of first, second and third PCA component vectors: a) major; b) intermediate; and c) minor axes orientation for representative ellipsoids in the lower hemisphere projections. The presented PCA components vectors are the same to those shown in Figure 3; d) time series for change of PCA component length (major, intermediate, and minor axes lengths); and e) the aspect ratio between the first to third PCA component length (red) and second to third PCA component length (yellow).

PCA analysis was conducted on the microseismic data in the post-injection phase. Microseismic activity in the post-injection phase was significant only a few days following the shut-in, and then the seismic activity had nearly ceased. Therefore, a dynamic change in MS cloud growth was not observed (Figure S2). Figure 5 shows the time series changes of the three PCA components for every ten days. Based on Figure 5(a)–5(c), the orientation of each PCA component was almost constant. The first PCA component was nearly vertical, and the second component was virtually identical to the orientation of S_{Hmax}. The third PCA component was consistent with the orientation of S_{hmin} during stimulation. Therefore, we observed a significant transition of MS cloud growth behavior during and after stimulation. In the first 14 d of the post-injection phase, which had begun 6.5 d from the commencement of injection, the MS cloud had the greatest extension. The first PCA component was significantly extended, causing a greater distinction to the second PCA component (Figure 5(c)). After 20 d, the MS cloud was slightly extended, and the orientation of the PCA components was also stable. It should be noted that most of the microseismic activity during the post-injection phase was observed in the shallow part of the reservoir (Figure 2(d)). Due to the small number of events, PCA analysis is not performed for incremental data.

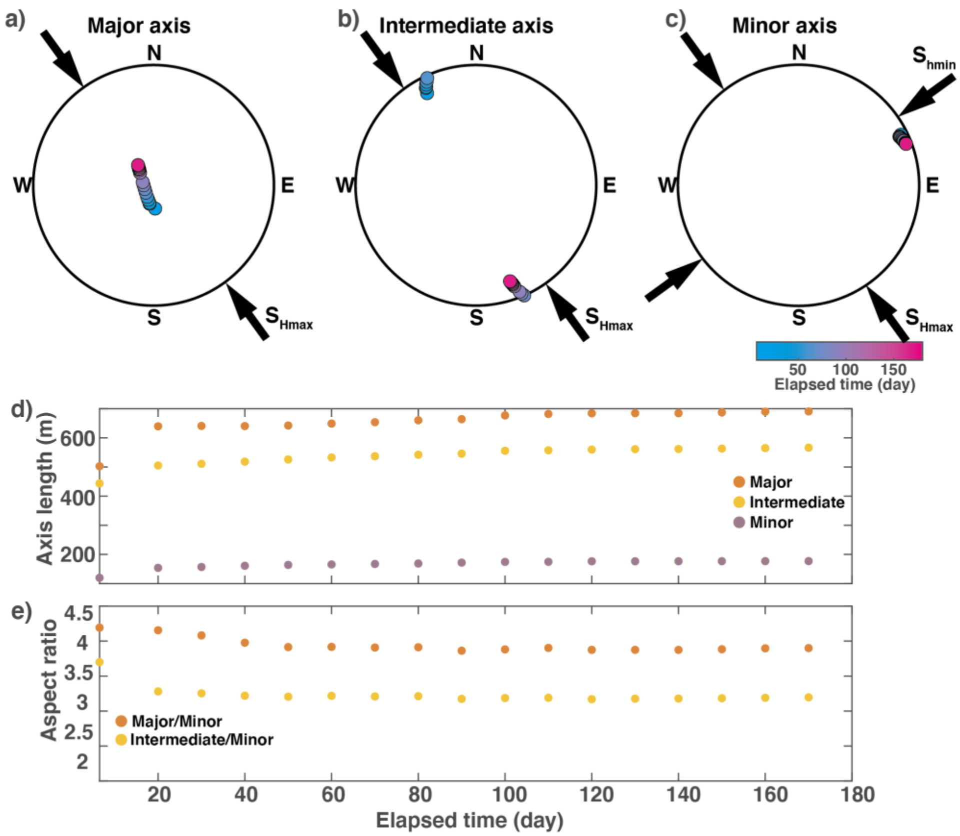

Figure 5. The results of PCA analysis for the MS cloud during the post-injection phase. All panels are shown in the same manner as Figure 4.

3.2 Depth sectional MS cloud growth

We investigated the MS cloud shape further at different depths and examined the influence of depth dependent *in-situ* stress. We applied PCA to microseismic events from a 100 m width different depth section. We computed only two PCA components, ignoring depths of each microseismic event. Each depth section for this analysis did not overlap, and microseismic events that occurred from the same vertical existing fault were contained over several depth sections. In addition to the PCA components, the geometric relationship between the gravity point of the MS cloud to each hypocenter was summarized as a rose diagram in a subset for each panel of Figure 6.

We observed a very linear MS cloud shape in the shallower part of the reservoir (4000–4200 m), where almost no variation in the fracture was delineated by microseismicity. From ~4200 m, we observed that the MS cloud had begun thickening by the events that occurred from different fractures. These features resulted in the extension of the second PCA component and an elliptical shape for the entire MS cloud. This tendency was also observed in the MS cloud at deeper depths (4200–4700 m). In the 4300–4400 m depth section, the MS cloud was very sparse, and the rose diagram showed very different shapes to those at shallower depths. Seismic activity was observed in branch fractures striking EW at 4400–4500 m. At this depth, the northern MS cloud appeared independent of the main and southern parts of the MS cloud. In the next depth section of 4500–4600 m, the densest seismic activity moved slightly north, as demonstrated by the gravity point of the MS cloud. In the deeper part of the reservoir, the MS cloud was divided into northern and southern parts by the aseismic region.

Despite the depth dependent features of microseismic activity and associated MS cloud shape, the macroscopic trend of the MS shape had been maintained as the MS cloud extended the orientation almost identical to the S_{Hmax}. Figure 7(a) summarizes the azimuths of the first PCA component variation and depth, and shows that the azimuth of the first PCA component had slightly rotated from north to east, with an increase in depth. This rotation may be attributed to the difference in microseismic activity at each depth. We visualized the existing fractures delineated by multiplet analysis (clustering analysis) at each depth in Figure S3. The aspect ratios of the MS cloud at each depth were between two and four, with the exception of depths at 4700–4800 m, as shown in Figure 7. At shallower depths, the aspect ratios exceeded 6; these exceptionally high aspect ratios reflect the linear shape of the MS cloud at shallower depths. It should be noted that the majority of the events from ~4200 m occurred following the shut-in operation.

As we investigated the MS cloud shape in different depth sections ignoring depth, we estimated the horizontal stress ratio defined as $(S_{Hmax}-p_{hyd})/(S_{hmin}-p_{hyd})$ in each depth (Figure 7(b)); this was around 2.3 in the reservoir depth (Figure 7(c)). The horizontal stress ratio was not the same as the aspect ratio of the MS cloud, although it is fairly consistent with the aspect ratio from the MS cloud growth except for the shallow two sections.

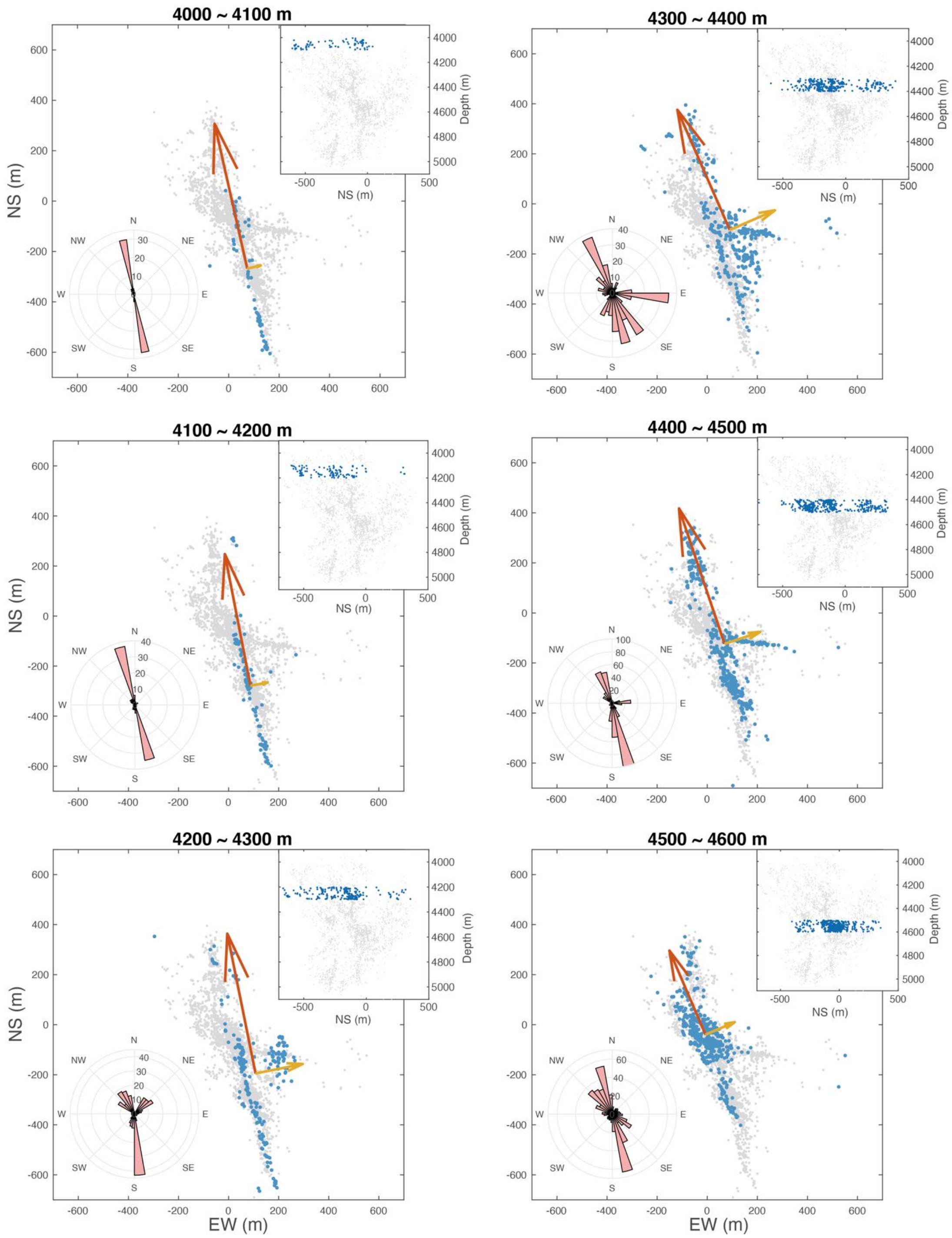

Figure 6. Hypocenter distribution of events for different 100 m depth sections in horizontal view. The blue dots are the event hypocenter in the target depth. The results of the 2D PCA analysis are shown with two arrows. The right shoulder inset is an NS cross section showing the target depth. The gray dots denote all microseismic events. The left lower inset represents the rose diagram for geometrical orientations from the gravity point of target events to each event.

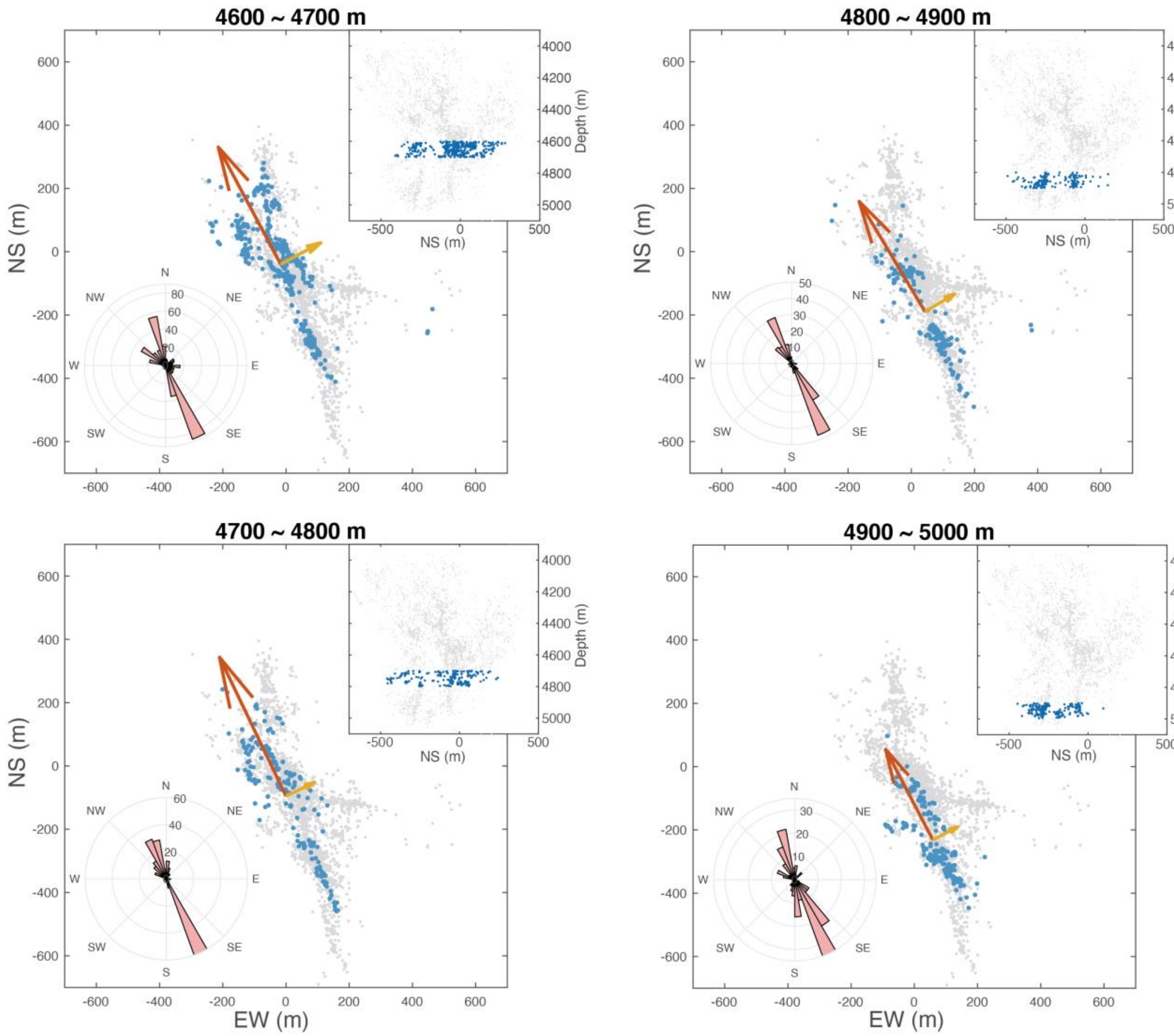

Figure 6. (continued).

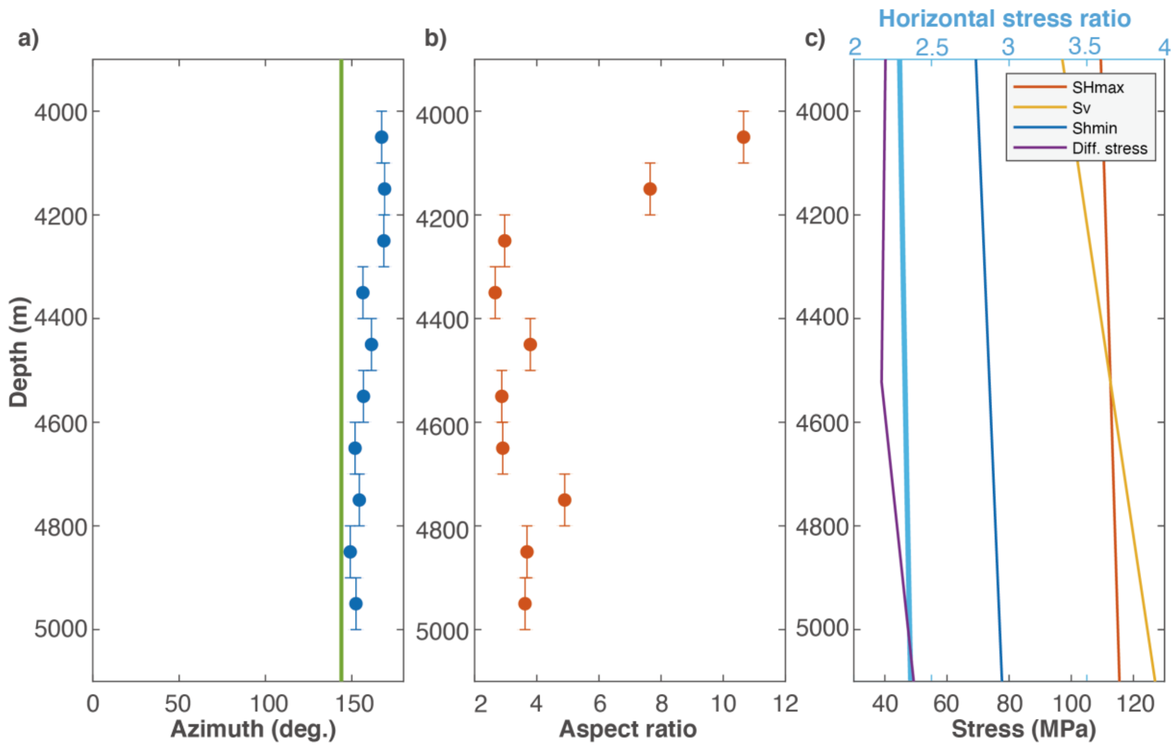

Figure 7. a) Orientation of the first component of PCA analysis as a function of depth. The vertical bar indicates the depth section for analysis. The vertical green line shows the orientation of S_{Hmax}; b) the aspect ratio between the lengths of the first and second components; and c) stress profile in study depth with horizontal stress ratio $(S_{Hmax}-p_{hyd})/(S_{hmin}-p_{hyd})$.

3.3 Injection depth MS cloud growth

During injection, the injected pore pressure migrated from the feed point in the well to the formation. The pore pressure decayed with distance from the injection point based on the permeabilities of existing fractures of the flow path, connectivity of those, and injection pressure. Thus, pore pressure migration is a complicated and nonlinear phenomenon. It may be reasonably assumed that the pore pressure in the vicinity of the injection point was as high as that at the injection point, or the pore pressure decay was relatively small. Therefore, we may forecast that the MS cloud shape near the injection point was linear or simple during the initial stage of stimulation as only well oriented fractures may experience shear failure. Later, more non-optimally oriented existing faults cause shear slip as pore pressure increases, making the MS cloud more spherical in shape. We investigated the time series change of MS cloud shape with injection depth based on this working hypothesis.

We focused on an event that occurred between 4500 and 4700 m, including the main feed point of the cataclastic fracture zone (Häring et al., 2008). Microseismic events during the early stage of stimulation also occurred at this depth. We focused on an NS >-200 as we observed that the southern part of the MS cloud was divided by the aseismic zone and not directly connected to the injection zone in 3.2 (Figure 6). We applied 2D PCA to a time series of MS cloud growth at every 0.5 d (Figure 8). The MS cloud had been drop-shaped, extending to NW until 3.5 d of the stimulation, from which it displayed greater linearity. After 3.5 d, the MS cloud became thicker with time, and its shape became more elliptical. Time incremental analysis result is shown in

Figure S4. The relative geometry to the MS cloud gravity point is summarized in Figure 9(a) in the same manner as Figure 6. The contribution to whole MS cloud shape from each existing fracture is delineated with the microseismic clusters (Figure S5).

The time series change in the first and second PCA components and their lengths are also summarized in Figure 9b. The rose diagram shape and orientation of the PCA components varied slightly with time. During the stimulation phase, the rose diagram shape had somewhat changed, suggesting that more events occurred in the north direction. The orientation of the first PCA component was more or less stable during stimulation. The aspect ratio increased gradually, reflecting a more linear MS cloud shape during the early stage of the stimulation. After 2.5 d, this ratio decreased as the MS cloud became thicker; the aspect ratio varied between 2.5 and 3.5. Note that the horizontal stress ratio (p_{hyd} deducted) in this depth section was approximately 2.34.

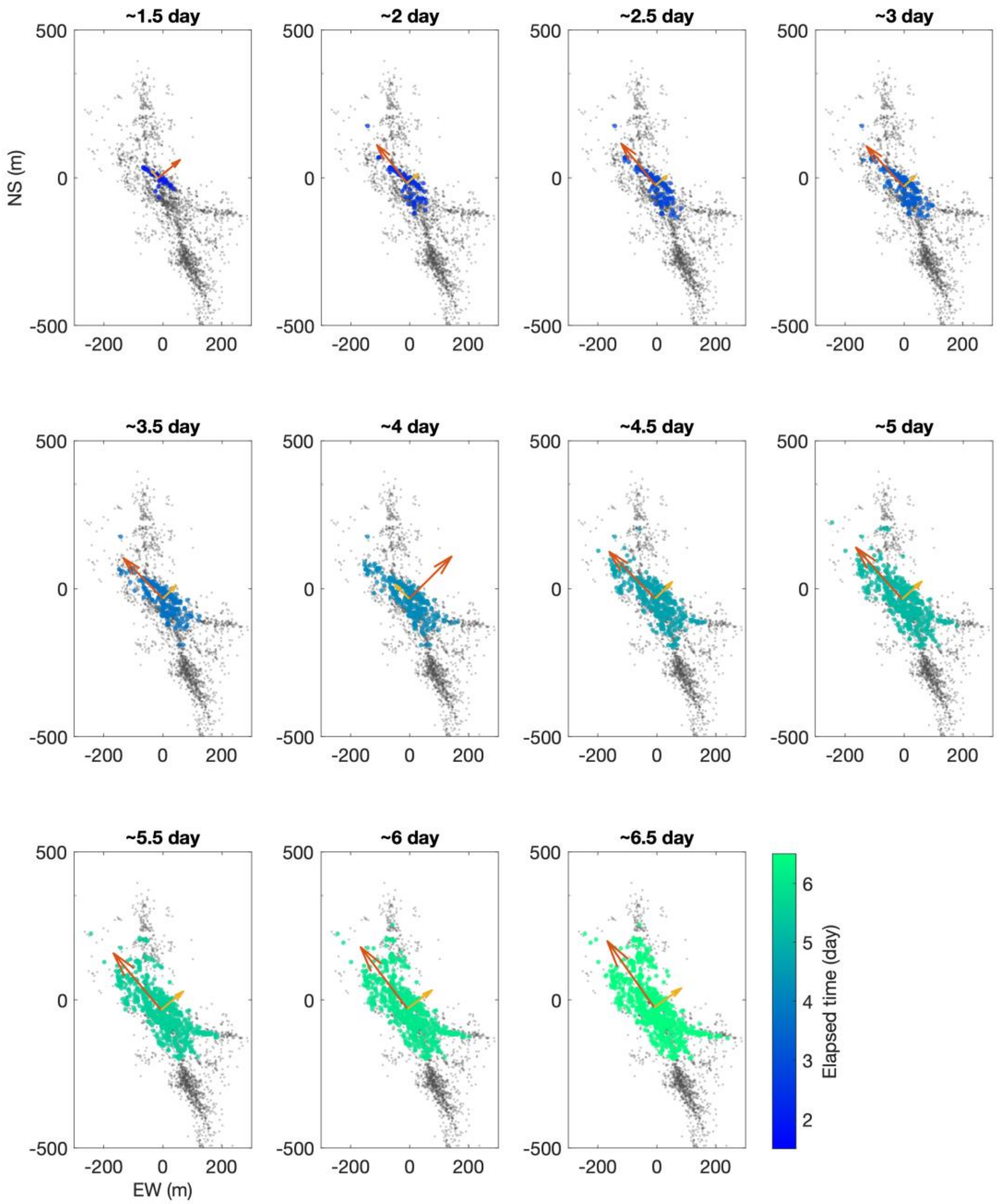

Figure 8. Time series evolution of microseismic events at an injection depth of 4500~4700 m. The 2D PCA results are shown with two arrows; red: first component, yellow: second component.

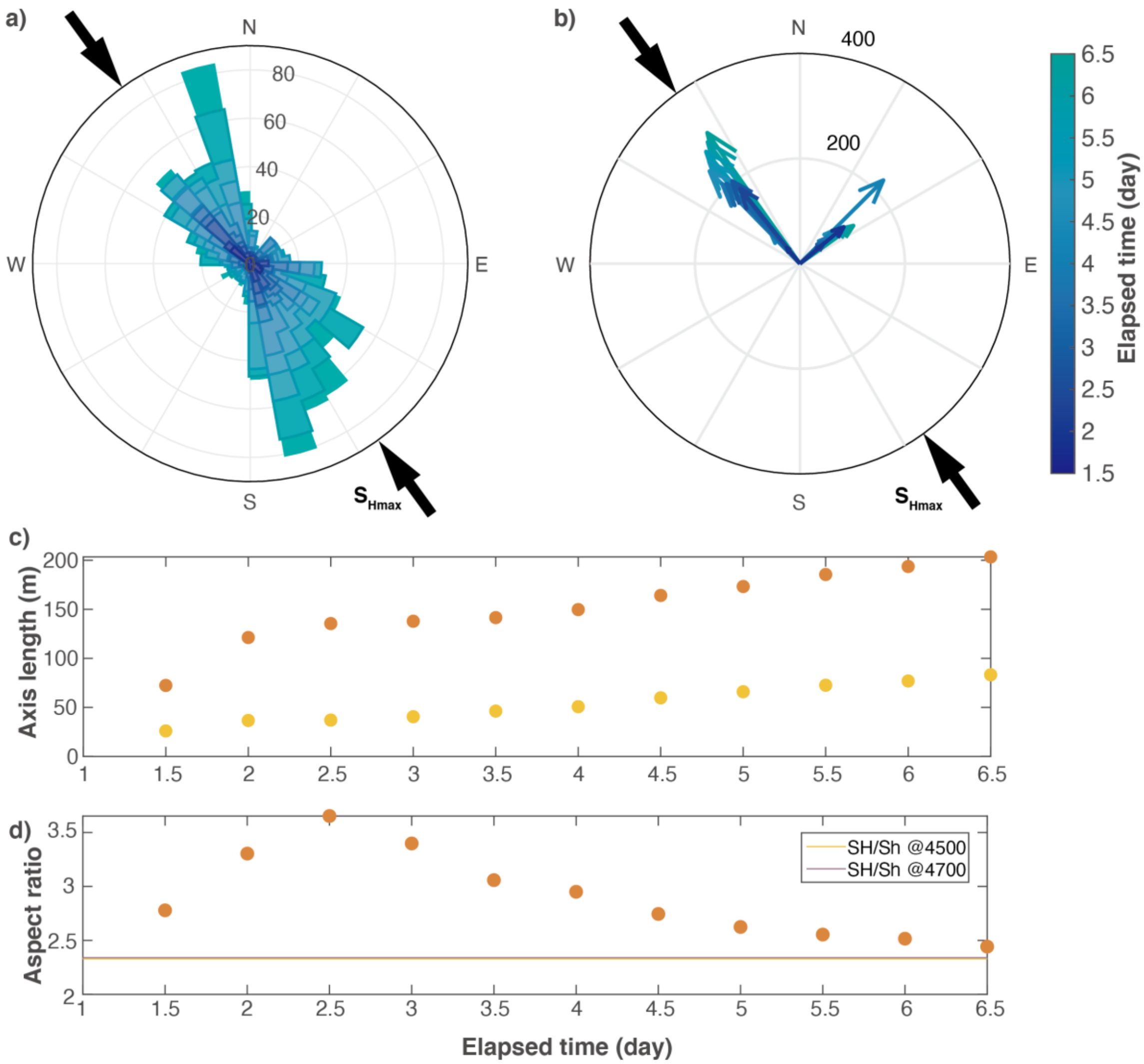

Figure 9. a) Rose diagram of geometrical orientations from gravity point to each event. The color of the rose diagram corresponds to the analysis time; b) time series change of orientation and length of first and second component of PCA. Color correlates analysis time; c) length of first and second components of PCA analysis as a function of time; d) aspect ratio of first and second components of PCA analysis as a function of time compared with horizontal stress ratio at 4500 and 4700 m.

3.3 Cross sectional MS cloud growth

We observed the cross-sectional MS cloud growth along N144°E (N36°W), which is the orientation of S_{Hmax}. By visual inspection, the orientation that microseismic events distributed most was not always the orientation of S_{Hmax} (Mukuhira et al., 2017). Based on the results of PCA analysis performed in 3.1, and to investigate the influence of S_{Hmax}, we chose S_{Hmax} orientation. Fig. 10 shows the time series evolutions of the MS cloud along the N36°W cross section. We selected events that occurred within ± 200 m from N36°W for this analysis (Figure S6). Incremental time series analysis is shown in Figure S7 and multiplet analysis result in this manner is also shown in Figure S8.

In the first three time steps up to 2.5 days, the 1st PCA component was nearly vertical, and the lengths of both the 1st and 2nd PCA components were close to each other. On the 3rd day, one of the components started dipping. The lengths of 1st and 2nd PCA components were competitive, so that the transition between 1st and 2nd PCA components occurred at 3.5, 4.5, and 6 days. The PCA component showed different behavior at the time step of 6.5 days and the 1st PCA component oriented nearly vertically. These observations are the same as those from three-dimensional observations in 3.1. In addition to the PCA results, we confirmed that the MC cloud shape was a more or less circular shape. The aspect ratio was between 1–1.3 more stable than that in the case of depth sectional observation (Figure 11(a)). The ratio between S_{Hmax} and Sv was 1–1.15 in the target depth section (4200–5000 m), even though the stress transition occurs from the strike-slip regime to the normal fault regime at around 4500 m (Figure 11(b)).

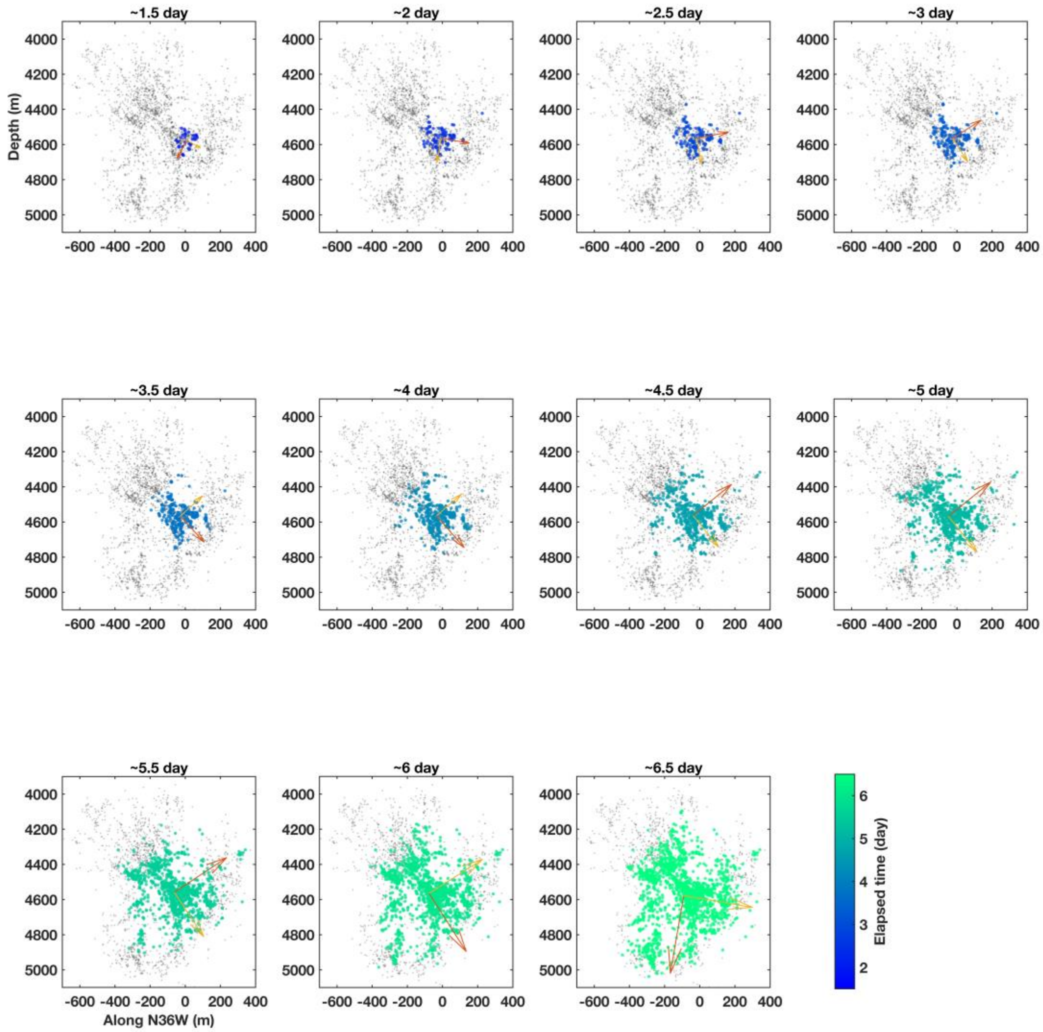

Figure 10. Time series evolution of microseismic events along the N35°W until 6.5 days from the stimulation start. Events that occurred ± 200 m along N36°W were plotted and analyzed. The 2D PCA analysis results are shown with two arrows (red: 1st, yellow: 2nd components).

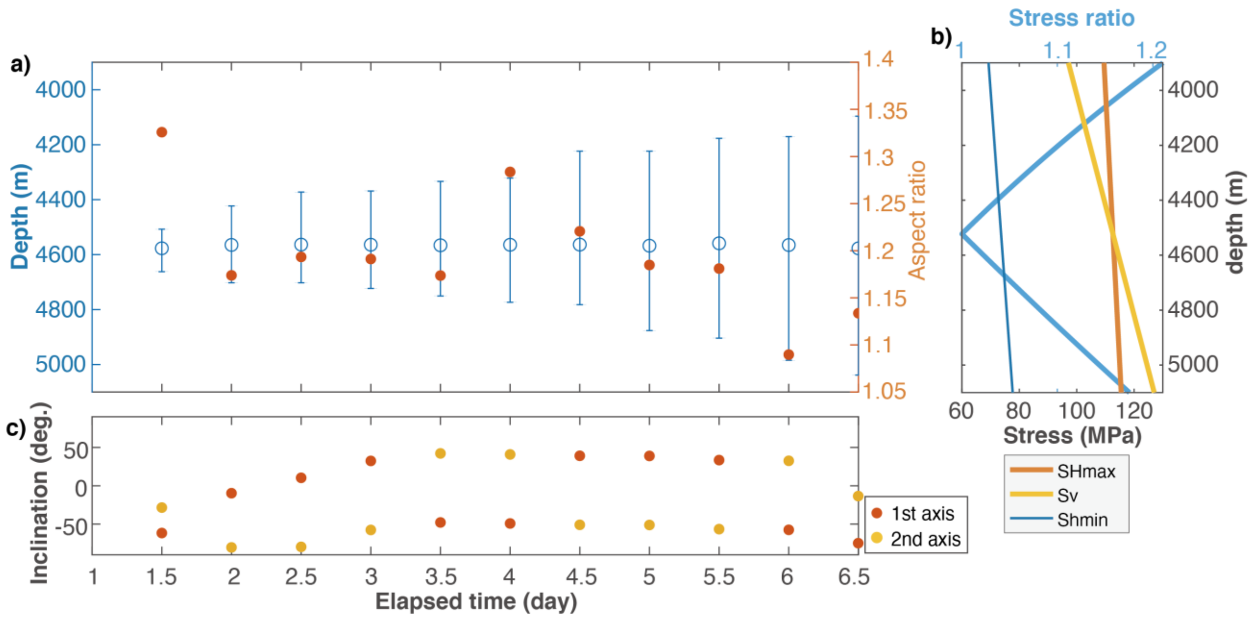

Figure 11. Correlation between MS cloud shape and in-situ stress. a) Circles corresponds to the gravity depth of the MS cloud, and the error bar corresponds to the upper and lower limits of the MS cloud. Red dots show the aspect ratio of the 1st and 2nd components of MS cloud. b) stress profile and stress ratio between vertical and maximum horizontal stress. c) inclination of 1st and 2nd component. Downdip is negative in this figure.

4 Discussion

4.1 Permeability tensor delineated by MS cloud growth

We observed a significant change in the PCA component directions before and after the reduction of flow rate or shut-in. Dipping the first PCA component had become more vertical and remained constant after the shut-in. The first and second PCA component lengths were competitive during stimulation. The vertical expansion of the MS cloud after shut-in was attributed to the extension of the first PCA component and rotation of the first and second PCA component directions. PCA was applied for all events that had occurred during and after the shut-in. However, PCA applied to the MS cloud after the shut-in was also able to extract MS cloud growth well. The events that occurred during stimulation did not influence the PCA for the event that occurred after the shut-in because of the closeness of the first and second PCA components. Note that the third PCA component was constantly oriented to S_{hmin} for the entire study period.

The shape of the MS cloud was interpreted as three orthogonal vectors of permeability. We observed MS cloud growth as a result of pore pressure migration controlled by permeability in the reservoir. In a fractured reservoir, each fracture has a different permeability according to its geometry to the stress regime. It is reasonable to regard the aggregation of permeabilities of existing fractures as apparent permeability of the entire reservoir in a macroscopic way. Thus, three PCA components may be considered an effective permeability tensor in three dimensions. This is a similar concept to the diffusivity tensor proposed by Shapiro et al. (1999). In our case, the underlying physical and hydrological model is fluid flow in the fracture system as opposed to anisotropic porous media. We do not intend to estimate the permeability tensor quantitatively, although we investigate its qualitative features and its correlation to *in-situ* stress.

The transition of PCA component direction, the proxy of permeability tensors, suggests that the apparent permeability tensors had significantly changed before and after the shut-in. This indicates that the apparent permeability tensor delineated by MS cloud growth differed during and after stimulation. During stimulation, due to the injection, even a non-optimally oriented fault may experience shear slip in addition to optimally oriented faults. Thus, the pore pressure migrates an optimally oriented fault that is more permeable and a non-optimally oriented, less permeable fault. As such, during the stimulation, the MS cloud reflected all microseismic events from those faults, and we observed the permeability tensor under dynamically pressurized conditions. Therefore, we refer to this dynamic permeability tensor. Following stimulation or shut-in, despite the occurrence of a very dynamic pore pressure re-distribution process associated with shut-in over a few days (Mukuhira et al., 2017), the pore pressure relaxation occurs with inherent reservoir permeability because of the disappearance of the pressure source. Pore pressure migrates along naturally permeable fractures that are optimally oriented, and the most permeable faults.

4.2 MS cloud growth controlled by *in-situ* stress

Throughout the PCA and based on several observations, we found that the MS cloud shape was significantly correlated with *in-situ* stress. From the 3D MS cloud growth observation, the MS cloud extension did not always occur in the maximum principal stress direction. Rather, it occurred in the plane perpendicular to the minimum principal stress (S_{hmin}). It is difficult to perceive the 3D growth of the MS cloud for human inspection; however, we discovered that MS cloud growth occurred in the direction influenced by maximum and intermediate principal stress. Previously, the MS cloud was considered to extend in the maximum principal stress direction. Although this is correct the insights from this study show that the MS cloud does not extend exactly to the maximum principal stress, rather, it extends in the plane defined by the maximum and intermediate principal stress, keeping the balance of maximum and intermediate stress. The influence of intermediate stress could not be ignored. Throughout our study period, the third PCA component was constantly oriented in the S_{hmin} direction (Figures 4(c) and 5(c)), regardless of the scale change of the MS cloud over time. This suggests that MS cloud growth behavior in this field is a scale-independent process, and indicates the homogeneity of *in-situ* stress in the reservoir.

From the depth sectional PCA analysis (Figures 6 and 7), the MS cloud extension orientation was more or less constant and consistent with the orientation of S_{Hmax} despite the influence of various existing faults in each depth section (Figure S3). The 2D aspect ratios at each depth were also stable and showed similar values to the horizontal stress ratio, with the exception at shallower depths (~4300 m). Most MS events at shallower depths occurred after the shut-in (Figure 2). A tiny perturbation of pore pressure triggered these events, such that the delineated MS cloud was the optimally oriented fracture that presented a higher aspect ratio. Thus, the shape of the MS cloud is also influenced by pore pressure migration.

Observations from the injection depth section further support this observed tendency. The orientation of the MS cloud was stable and the same as that of S_{Hmax}. The MS cloud shape was more linear during the early stage of stimulation as the pore pressure remained low, and optimally oriented faults were able to fail. Then, the MS cloud shape became more elliptical with time; i.e., pore pressure increase, because the non-optimally oriented fault could fail. Figure 9(d) shows a clear tendency that the aspect ratio of the MS cloud decreases with time (i.e., pore pressure). We conducted this analysis in the injection depth section, assuming that pore pressure in this depth section can become as high as wellhead pressure; a very strong pressure gradient in this section was not expected.

Time series observations on the cross-sectional MS cloud growth provides further evidence of the MS cloud growth dependence on *in-situ* stress. S_{Hmax} and S_v are the principal stressors working on this cross-section, and their stress magnitudes were very similar such that the stress regime transition occurs. The MS cloud aspect ratio was between 1.0 and 1.4, similar to the stress ratio between S_{Hmax} and S_v. The aspect ratio of the MS cloud did not change significantly compared to other aspect ratio observations. These observations suggest that pore pressure along this plane migrated radially, resulting in a circular MS cloud.

Thus, we found that MS cloud shape in our research field was mainly controlled by *in-situ* stress from the macroscopic perspective. Locally, the pore pressure perturbation or existing fracture affects the MS cloud shape, although this shape may be scaled with the principal stress ratio. We have not interpreted all of these local interactions as it was not easy to link to all physical processes associated with MS activity and *in-situ* stress, e.g., multiplet cluster analysis shown in Figure S5 or S8 is not very informative for our purpose due to its complexity. However, our analysis results reasonably imply the scaling relationship between MS cloud shape and *in-situ* stress. In this field, there were also various natural fractures from borehole logging analysis (Ziegler & Evans, 2015). Some of these fractures were connected to fractures delineated by microseismic analysis (Ziegler & Evans, 2020). Some existing fractures were orientated to that of the S_{hmin}. Therefore, it is likely that there was some flow path to the orientation of S_{hmin}. However, the extension of the MS cloud to the orientation of S_{hmin} was insignificant. These faults should not be very permeable due to high normal stress working on those fractures perpendicular to S_{Hmax}. Therefore, we conclude that *in-situ* stress plays a primary role in controlling the MS cloud growth associated with pore pressure migration. This is achieved by controlling the permeability and shear failure of each existing fracture in a fractured reservoir that hosts a wide variety of existing fractures.

4.3 Comparison with other EGS field

In this section we discuss how the insights derived from this study may explain the MS cloud growth in other EGS fields. We select a number of the cases of EGS and HDR projects and review the MS cloud growth features by comparing the *in-situ* stress information based on published literature. The reliability of microseismic and *in-situ* stress information is very site dependent, and the project year also impacts reliability based on the technologies available at that time.

4.3.1 Soultz-sous-Forêts, France

Hydraulic fracturing was conducted at GPK-1 in the Soultz-sous-Forêts HDR field, located in the Rhine graben with a basement of Soultz granite having intruded the Devonian-Early Carboniferous rocks. For 20 d in 1993, ~45,000 m^3 of freshwater was injected into granite. This was done at depths between 2.8 and 3.4 km with a maximum wellhead pressure of 10 MPa, whilst the flow rate was increased to 50 L/s (Baria et al., 1999; Moriya et al., 2002). The subvertical cloud of microseismicity that was 0.5 km wide, 1.2 km long, 1.5 km high and oriented N25°W was produced (Evans et al., 2005).

The orientation of the maximum principal horizontal stress, S_{Hmax}, obtained from thermally induced tension fractures in borehole GPK-1, was relatively well determined as N170°E ± 15° (Evans et al., 2005). The magnitudes of the maximum and intermediate principal stresses also shared similar values. The maximum principal stress direction was replaced from the horizontal direction to the vertical direction at a depth of approximately 2900 m, suggesting the closeness of S_{Hmax} and Sv. The minimum principal stress direction was estimated to be approximately N65°E.

The orientation of natural fractures detected by the UBI log run in GPK-1 indicates the dominance of subvertical fractures with strike of N-S. On the other hand, the MS cloud had the principal direction on the plane perpendicular to the minimum principal stress direction (N65°E). This implies that the shape and principal direction of the MS cloud were subject to tectonic stress as opposed to the orientation of natural fractures. These observations support the findings of this study, possibly because Soultz and Basel are within a similar tectonic setting.

4.3.2 Cooper Basin, Australia

First fluid injections were conducted in 2003 to create hot fractured rock geothermal reservoirs (Baisch et al., 2006). A total of 20,000 m^3 of fluid was injected into granite at 4250 m. More than 11,000 microseismic events delineated the sub-horizontal structure of the reservoir. The geometry of the MS cloud was 2 × 1.5 km in the horizontal direction and 150–200 m thickness. Horizontal MS cloud grew in the NNE-SSW direction. The reservoir consisted only of single or sub-parallel existing fractures based on the microseismicity and logging data (Baisch et al., 2006). The stress state was estimated to be the reverse fault regime, consistent with the overall MS cloud shape. However, the orientation of S_{Hmax} was N110°E (Reynolds et al., 2005), and this was not consistent with the orientation of MS cloud growth. The width of the MS cloud was significantly smaller than that of the horizontal extension, although detailed *in-situ* stress magnitude information was unavailable.

These observations were not always consistent with the insights of this study. However, the Cooper Basin may be interpreted as an extreme case of the site-specific condition of a very selective horizontal existing fracture; the existing fracture-dominated process. Therefore, in a field dominated by strongly preferred existing fractures, the insights from this study would be ineffective, as would the *in-situ* stress effect.

4.3.3 Fenton hill, United States

The massive hydraulic fracture treatment (MHF) on Well EE-2 was performed in 1983 as known as Expt. 2032. Roughly 21,000 m3 of water was injected at around 3.6 km depth. The maximum flow rate of 109 kg/s and maximum wellhead pressure of 4.9 MPa were recorded (Brown et al., 2012). MS cloud during MHF extended to NNW-SSE according to recent compiling work (Norbeck et al., 2018), despite the orientation of SHmax of N30°E. So, MS cloud growth of this field already showed unique behavior, which is different from the findings of this study, even though this is the first pilot project of EGS. The result of the wellhead pressure values of several pre-stimulations and focal mechanism leads to the orientation of dominant fracture sets as NNW-SSE (Norbeck et al., 2018). So, the MS cloud growth behavior was controlled by a more existing fracture set rather than in-situ stress. The in-situ stress magnitude information still has a room for investigation, injection pressure excessed the minimum principal stress, but still, MS cloud extended to a different direction to the maximum principal stress. Numerical experiment results suggest that the tensile-shear mixed mechanism and the existing fracture distribution played important role in the Fenton hill reservoir (Norbeck et al., 2018).

4.3.4 Desert Peak, United States

Desert peak is located in Hot Springs Mountain, Nevada, in the United States. Ormat Nevada Inc. conducted an enhanced geothermal systems project supported by DOE. In this project, multi-phased stimulations were conducted between 2010 and 2011 (Zemach et al., 2017). These stimulations were composed of hydroshearing (injection pressure < S_{hmin}), chemical fracking, and hydrofracking (injection pressure > S_{hmin}). The stimulation target was approximately 1000 m deep (Lutz et al., 2009). Microseismic events were mainly triggered during the hydrofracking phase, and formed a subvertical tabular shaped cloud based on the seismic event list in Zemach et al. (2017). The major and minor axes of the tabular cloud were ~1 km and corresponded to the S_v and S_{Hmax} directions (Davatzes & Hickman, 2009), respectively. The thickness direction of the tabular cloud was 0.2 km, along the S_{hmin} direction of the normal fault stress regime (Davatzes & Hickman, 2009). The stress magnitude at a depth of 930 m was estimated to be 22.6 MPa (S_v), 18.2–22.6 MPa (S_{Hmax}) and 13.8 MPa (S_{hmin}) (Hickman & Davatzes, 2010). The aspect ratios of the MS cloud and stress ratio were 1:1:0.2 and 1:0.8–1: 0.6, respectively. The MS cloud direction and aspect ratio were consistent with those of *in-situ* stress, consistent with the findings in this paper, although microseismic events occurred under hydrofracking conditions.

4.3.5 Pohang, South Korea

Pohang is located in the southeastern area of South Korea. The Pohang EGS project was terminated with the Pohang earthquake (Mw 5.5) on November 15, 2017 (Korean Government Commission, 2019; Ellsworth et al., 2019). Injection was conducted using two wells (PX-1 and PX-2) that were separated by several hundred meters. Injection from PX-2 seemed to induce the Pohang earthquake. Prior to the mainshock, the MS cloud around the injection point of PX-2 formed a tabular shape (strike N214°E, dipping 43°). On the other hand, the direction of *in-situ* S_{Hmax} was N77°E; this did not exactly correspond with the strike of the MS cloud. The lengths of the MS cloud along strike, dip and width directions were 1, 0.5 and 0.2 km, respectively based on the hypocenter location (Korean Government Commission, 2019; Ellsworth et al., 2019). The estimated stress magnitude at a 4.2 km depth was S_{Hmax} = 243 MPa, S_{hmin} = 120 MPa, and S_v = 106 MPa, suggesting normal faulting stress regime (Korean Government Commission, 2019; Ellsworth et al., 2019). Therefore, the shape of the MS cloud did not agree with the *in-situ* stress ratio. The MS cloud may have selectively occurred on an unknown fault, in turn triggering the mainshock (Korean Government Commission, 2019; Ellsworth et al., 2019).

4.3.6 Helsinki, Finland

In an EGS project in Helsinki, Finland, the first pilot stimulation was conducted at the OTN-3 well by St-1 Deep Heat Oy in 2018 (Kwiatek et al., 2019). They targeted the granitic formation at a true vertical depth of 5.7 to 6.1 km. At this depth, the principal stress magnitudes were estimated to be approximately S_{hmin} = 110 MPa, S_v = 180 MPa, and S_{Hmax} = 240 MPa. The pore pressure was assumed to be hydrostatic, and approximately 60 MPa, suggesting a critical stress state for shear slip occurrence at optimally oriented fractures.

The microseismicity of 1977 events was relocated by a relative location technique (Kwiatek et al., 2019). The hypocenter distribution delineated some spatially separated clusters in the vicinity of individual sections of multi-stage stimulation. The NW–SE trending macroscopic horizontal extension of each cluster was subparallel to the axis of the current local S_{Hmax} (N110°E). The majority of microseismicity was determined in a cluster around the bottom hole regardless of the active injection stage, due to the packer leak. This largest hypocenter cluster exhibited a plane-like shape dipping to the NE. Although the causes of this oblique hypocenter distribution were not revealed, the plane like flat shape of the hypocenter distribution possibly corresponds to an anisotropic stress ratio. The hypocenter clusters located in the shallower depth range from 4900–5900 m showed a horizontally linear shape with a horizontal aspect ratio of 1:3 (visually measured); this was consistent with the anisotropic horizontal stress ratio.

4.3.7 Hijiori, Japan

Following nearly aseismic first hydraulic fracturing in 1986, the second hydraulic stimulation that induced 65 events, in the third case, approximately 2115 m^3 of freshwater was injected into HDR-1 at a depth of 2.3 km in 1992 (Sasaki and Kaieda, 2002). Then, the source locations of 127 events were determined. The MS cloud shows several planar features; strike in the E-W direction, dipping in N direction. The lengths of the MS cloud along the strike, dip, and width directions were 0.5, 0.5, and 0.2 km, respectively (Tezuka and Niitsuma, 2000; Sasaki and Kaieda, 2002). The estimated stress magnitude at 2.2 km depth was S_{Hmax} = 64.8 MPa (E-W), S_{hmin} = 39.4 MPa (N-S), and S_v = 45 MPa (Oikawa and Yamaguchi, 2000). The principle direction of the MS cloud agreed with the S_{Hmax} direction, where the aspect ratios of the MS cloud and the stress ratio were 1:1:0.4 and 1:0.61:0.69 (p_{hyd} deducted), respectively.

The MS cloud direction was correlated to *in-situ* stress to a certain extent, although their aspect ratios were not correlated to *in-situ* stress ratio fully. Note that the number of microseismic events was significantly small compared to other cases, regardless of the moderate wellhead pressure of 26 MPa for third hydraulic fracturing.

4.3.8 Ogachi, Japan

Hydraulic fracturing was conducted at OGC-1 in the Ogachi HDR field in Japan. Approximately 10,140 m^3 of freshwater was injected into granodiorite between 0.99 and 1.0 km depth in 1991. Then, approximately 5440 m^3 of freshwater was injected between 0.71 and 0.72 km depth in 1992 (Kaieda et al., 1992; Hori et al., 1994; Kaieda et al., 2010). During the first hydraulic fracturing, the source locations of 1554 events were determined, and an MS cloud that was 0.2 km wide, 1 km long, 0.5 m high, and oriented N20°E was produced. In the second hydraulic fracturing, the source locations of ~1000 events were determined, with an MS cloud that was 0.2 km wide, 0.8 km long, 0.4 km high, and oriented N100°E (Hori et al., 1994). The estimated stress magnitude at a 0.99~1.0 km was S_{Hmax} = 25 MPa (E-W), S_{hmin} = 22 MPa, and S_v = 25 MPa. This suggests a reverse or strike-slip faulting stress regime. The magnitudes of S_{hmin} and S_v shared similar values, and their size relation is likely to be interchanged (Shin et al., 2000).

During the first hydraulic fracturing, the principal direction of the MS cloud did not agree with the S_{Hmax} direction (E-W). This suggests that the shape of the MS cloud growth was potentially controlled by pre-existing fractures as opposed to tectonic stress. In the second hydraulic fracturing, the principal direction of the MS cloud agreed with the maximum principal stress direction, although the aspect ratios of the MS cloud and stress ratios were 1:0.5:0.25 and 1:0.6: 0.5, respectively. The MS cloud direction and aspect ratio were correlated to those of *in-situ* stress to a certain extent, although the MS cloud extended to the direction of the minimum principal stress compared to the forecasted *in-situ* stress.

5 Conclusions

This study precisely investigated how microseismic clouds grow during hydraulic stimulation by applying PCA to a time series of microseismic hypocenter distribution. PCA derived the orientation of MS cloud growth both quantitatively and statistically. The MS cloud behavior characterized by PCA in several aspects was compared and discussed as it relates to *in-situ* stress information.

The main conclusions of this study were:

- The MS cloud growth behavior differed during and after stimulation, corresponding to the dynamic and static permeability tensor of the reservoir. During stimulation, the MS cloud shape changed with an increase in pore pressure, controlled by the *in-situ* stress. In post-stimulation, the MS cloud extended along the optimally oriented fractures, which were the most permeable;
- The MS cloud shape and its aspect ratio defined in the horizontal or cross-sectional direction matched very well with the effective stress ratio on that plane. The MS cloud from different depth sections showed a close aspect ratio to the effective horizontal stress ratio. Depth section and cross-sectional MS cloud along the orientation of S_{Hmax} was circular, reflecting the very close stress magnitude of S_{Hmax} and S_v;
- Insights from this study were compared to MS cloud shapes from different EGS fields. Many of the fields showed satisfiable consistency between MS cloud shape and *in-situ* stress.

We conclude that MS cloud shape is mainly controlled by *in-situ* stress, particularly in where various existing fractures exist, such as was the case in Basel. This study has advanced the understanding of the reservoir creation process. There are still knowledge gaps that need to be addressed for a complete understanding of the reservoir creation process. These include understand how the MS cloud shape may be roughly scaled by the stress ratio. The findings from this study also emphasize the importance of reliable stress measurements that provide more meaningful information on the reservoir creation process.

Acknowledgments, Samples, and Data

All authors are not aware of any conflicts of interest. We thank N. Watanabe for discussions and comments on the manuscript. This study is supported by an R&D project for super-critical geothermal field development supported by NEDO. Part of the work was carried out under the Collaborative Research Project of the Institute of Fluid Science, Tohoku University.

Data Availability Statement

The microseismic catalog data containing the location, magnitude, and cluster information is uploaded to the MIT institutional repository associated with submission of another paper (under review) to AGU journal. Meanwhile, data are temporarily available in the Supporting Information.

References

Asanuma, H., Kumano, Y., Hotta, A., Niitsuma, H., Schanz, U., & Häring, M. (2007), Analysis of microseismic events from a stimulation at Basel, Switzerland, *GRC Transactions*, *31*, 265–270.

Asanuma, H., Kumano, Y., Niitsuma, H., Schanz, U., & Häring, M. (2008). Interpretation of Reservoir Structure from Super-Resolution Mapping of Microseismic Multiplets from Stimulation at Basel, Switzerland in 2006, *Procedings of the World Geothermal Congress*.

Baisch, S., Weidler, R., Vörös, R., Wyborn, D., & de Graaf, L. (2006). Induced seismicity during the stimulation of a geothermal HFR reservoir in the Cooper Basin, Australia. *Bulletin of the Seismological Society of America*, *96*(6), 2242–2256. https://doi.org/10.1785/0120050255.

Baria, R., Baumgärtner, J., Gérard, A., Jung, R., & Garnish, J. (1999). European HDR research programme at Soultz-sous-Forets (France) 1987-1996. *Geothermics*, *28*(4–5), 655–669. doi:10.1016/S0375-6505(99)00036-X.

Brown, D., Duchane, D., Heiken, G., Hriscu, V. (2012). Mining the Earth's Heat: Hot Dry Rock Geothermal Energy. Springer.

Davatzes, N., & Hickman, H. (2009). Fracture, stress and fluid flow prior to stimulation of well 27-15, Desert Peak, Nevada, EGS project, *Proceedings of the 34th Workshop on Geothermal Reservoir Engineering*, Stanford, CA.

Dyer, B. C., Schanz, U., Ladner, F., Häring, M. O., & Spillman, T. (2008). Microseismic imaging of a geothermal reservoir stimulation. *The Leading Edge*, *27*(7), 856. doi: 10.1190/1.2954024.

Dyer, B. C., Schanz, U., Spillmann, T., Ladner, F., & Häring, M. O. (2010). Application of microseismic multiplet analysis to the Basel geothermal reservoir stimulation events. *Geophysical Prospecting*, *58*(5), 791–807. doi:10.1111/j.1365-2478.2010.00902.x.

Ellsworth, W. L., Giardini, D., Townend, J., Ge, S., & Shimamoto, T. (2019). Triggering of the Pohang, Korea, earthquake (Mw 5.5) by enhanced geothermal system stimulation, *Seismological Research Letters*, *90*, 1844–1858.

Evans, K. F., Moriya, H., Niitsuma, H., Jones, R. H., Phillips, W. S., Genter, A., et al. (2005). Microseismicity and permeability enhancement of hydrogeologic structures during massive fluid injections into granite at 3 km depth at the Soultz HDR site. *Geophysical Journal International*, *160*(1), 388–412. doi:10.1111/j.1365-246X.2004.02474.x.

Häring, M. O., Schanz, U., Ladner, F., & Dyer, B. C. (2008). Characterisation of the Basel 1 enhanced geothermal system. *Geothermics*, *37*(5), 469–495. doi: 10.1016/j.geothermics.2008.06.002.

Herrmann, M., Kraft, T., Tormann, T., Scarabello, L., & Wiemer, S. (2019). A Consistent High-Resolution Catalog of Induced Seismicity in Basel Based on Matched Filter Detection and Tailored Post-Processing. *Journal of Geophysical Research: Solid Earth*, *124*(8), 8449–8477. doi:10.1029/2019JB017468.

Hickman, S., & Davatzes, N. C. (2010). In-situ stress and fracture characterization for planning of an EGS stimulation in the Desert Peak Geothermal Field, Nevada, *Proceedings of the 35th Workshop on Geothermal Reservoir Engineering*, Stanford, CA.

Hill, D. P. (1977). A model for earthquake swarms. *Journal of Geophysical Research*, *82*(8), 1347. doi:10.1029/JB082i008p01347.

Hori, Y., Kitano, K., & Kaieda. (1994). Outline of Ogachi project for HDR geothermal power in Japan, *Transactions of the Geothermal Resources Council*, *18*, 439–443.

Kaieda, H. et. al. (1992). Ogachi project for HDR geothermal power in Japan first hydraulic fracturing results, *Transactions of the Geothermal Resources Council*, *16*, 493–496.

Kaieda, H., Sasaki, S., & Wyborn, D. (2010).Comparison of characteristics of microearthquakes observed during hydraulic stimulation operations in Ogachi, Hijiori and Cooper Basin HDR projects, *Proceedings of the World Geothermal Congress*.

Korean Government Commission. (2019). Summary report of the Korean Government Commission on relations between the 2017 Pohang Earthquake and EGS Project, Geological Society of Korea, Seoul, South Korea, doi: 10.22719/KETEP-20183010111860.

Kwiatek, G., Saarno, T., Ader, T., Bluemle, F., Bohnhoff, M., Chendorain, M., et al. (2019). Controlling fluid-induced seismicity during a 6.1-km-deep geothermal stimulation in Finland. *Science Advances*, *5*(5), 1–12. doi: 10.1126/sciadv.aav7224.

Lutz, S. J., Hickman, S., Davatzes, N., Zemach, E.,Drakos, P., & Robertson-Tait, A. (2010). Rock Mechanical Testing and Petrologic Analysis in Support of Well Stimulation Activities at the Desert Peak Geothermal Field, Nevada. *Proceedings of the 35th Workshop on Geothermal Reservoir Engineering*, Stanford, CA.

Moriya, H, Niitsuma, H., & Baria, R. (2003). Multiplet-Clustering Analysis Reveals Structural Details within the Seismic. *Bulletin of the Seismological Society of America*, *93*(4), 1606–1620. doi:10.1785/0120020072.

Moriya, Hirokazo, Nakazato, K., Niitsuma, H., & Baria, R. (2002). Detailed fracture system of the Soultz-sous-Forêts HDR field evaluated using microseismic multiplet analysis. *Pure and Applied Geophysics*, *159*(1–3), 517–541. doi:10.1007/PL00001263.

Mukuhira, Y., Dinske, C., Asanuma, H., Ito, T., & Häring, M. O. (2017). Pore pressure behavior at the shut-in phase and causality of large induced seismicity at Basel, Switzerland. *Journal of Geophysical Research: Solid Earth*, *122*(1), 411–435. doi:10.1002/2016JB013338.

Mukuhira, Y., Fuse, K., Naoi, M., Fehler, M. C., Moriya, H., Ito, T., et al. (2018). Hybrid focal mechanism determination: Constraining focal mechanisms of injection induced seismicity using in situ stress data. *Geophysical Journal International*, *215*(2), 1427–1441. doi:10.1093/GJI/GGY333.

Mukuhira, Yusuke, Asanuma, H., Niitsuma, H., & Häring, M. O. (2013). Characteristics of large-magnitude microseismic events recorded during and after stimulation of a geothermal reservoir at Basel, Switzerland. *Geothermics*, *45*, 1–17. doi:10.1016/j.geothermics.2012.07.005.

Mukuhira, Yusuke, Moriya, H., Ito, T., Asanuma, H., & Häring, M. (2017). Pore pressure migration during hydraulic stimulation due to permeability enhancement by low-pressure subcritical fracture slip. *Geophysical Research Letters*, *44*(7), 3109–3118. doi:10.1002/2017GL072809.

Norbeck, J. H., McClure, M. W., & Horne, R. N. (2018). Field observations at the Fenton Hill enhanced geothermal system test site support mixed-mechanism stimulation. *Geothermics*, *74*(March), 135–149. doi:10.1016/j.geothermics.2018.03.003.

Oikawa, Y. & Yamaguchi, T. (2000). Stress measurement using rock core in an HDR field, *Proceedings of the World Geothermal Congress*, 3819–3822..

Pine, R. J., & Batchelor, A. S. (1984). Downward migration of shearing in jointed rock during hydraulic injections. *International Journal of Rock Mechanics and Mining Sciences & Geomechanics Abstracts*, *21*(5), 249–263. doi:10.1016/0148-9062(84)92681-0.

Reynolds, S. D., S. D. Mildren, R. R. Hillis, J. J. Meyer, and T. Flottmann (2005). Maximum horizontal stress orientations in the Cooper Basin, Australia: Implications for plate-scale tectonics and local stress sources, Geophys. J. Int. 160, 331–343.

Sasaki, S., & Kaieda, H. (2002). Obervation and Analysis of AE Events Accompanying Hydraulic Injection at the Hijiori Hot Dry Rock Site, *Journal of the Geothermal Research Society of Japan*, *24*(3), 245–265.

Shapiro, S. A., Audigane, P., & Royer, J. J. (1999). Large-scale in situ permeability tensor of rocks from induced microseismicity. *Geophysical Journal International*, *137*(1), 207–213. doi:10.1046/j.1365-246X.1999.00781.x.

Shin, K., Ito, H., & Oikawa, Y. (2000). Stress state at the Ogachi site, *Proceedings World Geothermal Congress*, 1749–1752.

Sibson, R. H. (1996). Structural permeability of fluid-driven fault-fracture meshes. *Journal of Structural Geology*, *18*(8), 1031–1042. doi:10.1016/0191-8141(96)00032-6.

Soma, N., Niitsuma, H., & Baria, R. (2007). Reflection imaging of deep reservoir structure based on three-dimensional hodogram analysis of multicomponent microseismic waveforms. *Journal of Geophysical Research: Solid Earth*, *112*(11), 1–14. doi:10.1029/2005JB004216.

Tezuka, K & Niitsuma, H. (2000). Stress estimated using microseismic clusters and its relationship to the fracture system of the Hijiori hot dry rock reservoir, *Engineering Geology*, *56*, 47–62.

Valley, B., & Evans, K. F. (2009). Stress orientation to 5 km depth in the basement below Basel (Switzerland) from borehole failure analysis. *Swiss Journal of Geosciences*, *102*(3), 467–480. doi:10.1007/s00015-009-1335-z.

Valley, B., & Evans, K. F. (2015). Estimation of the Stress Magnitudes in Basel Enhanced Geothermal System. *World Geothermal Congress 2015*, (April), 12.

Valley, B., & Evans, K. F. (2019). Stress magnitudes in the Basel enhanced geothermal system. *International Journal of Rock Mechanics and Mining Sciences*, *118*(November 2018), 1–20. doi:10.1016/j.ijrmms.2019.03.008.

Waldhauser, F., & Ellsworth, W. L. (2000). A Double-difference Earthquake location algorithm: Method and application to the Northern Hayward Fault, California. *Bulletin of the Seismological Society of America*, *90*(6), 1353–1368. doi:10.1785/0120000006.

Watanabe, N., Hirano, N., & Tsuchiya, N. (2008). Determination of aperture structure and fluid flow in a rock fracture by high-resolution numerical modeling on the basis of a flow-through experiment under confining pressure. *Water Resources Research*, *44*(6), 1–11. doi:10.1029/2006WR005411.

Yeo, I. W., De Freitas, M. H., & Zimmerman, R. W. (1998). Effect of shear displacement on the aperture and permeability of a rock fracture. *International Journal of Rock Mechanics and Mining Sciences*, *35*(8), 1051–1070. doi:10.1016/S0148-9062(98)00165-X.

Zemach, E., Drakos, P., Spielman, P., & Akerley, J. (2013). Desert Peak Enhanced Geothermal Systems (EGS) Project (Draft Final Report), doi:10.2172/1373310.

Ziegler, M., Valley, B., & Evans, K.F. (2015). Characterisation of natural fractures and fracture zones of the Basel EGS reservoir inferred from geophysical logging of the Basel-1 well. *Proceedings of the World Geothermal Congress*, Melbourne, Australia, pp. 19–25. April, 12.

Ziegler, M., & Evans, K. F. (2020). Comparative study of Basel EGS reservoir faults inferred from analysis of microseismic cluster datasets with fracture zones obtained from well log analysis. *Journal of Structural Geology*, *130*(October 2019), 103923. doi:10.1016/j.jsg.2019.103923.

Zoback, M. (2007). Reservoir Geomechanics, Cambridge University Press.